

# High-Resolution Mapping of Dust via Extinction in the M31 Bulge

Hui Dong<sup>1,2</sup>, Zhiyuan Li<sup>3,4</sup>, Q. D. Wang<sup>5,3</sup>, Tod R. Lauer<sup>2</sup>, Knut A. G. Olsen<sup>2</sup>, Abhijit Saha<sup>2</sup>, Julianne J. Dalcanton<sup>6</sup>, Brent A. Groves<sup>7</sup>

<sup>1</sup> *Instituto de Astrofísica de Andalucía (CSIC), Glorieta de la Astronomía S/N, 18008 Granada, Spain*

<sup>2</sup> *National Optical Astronomy Observatory, Tucson, AZ, 85719, USA*

<sup>3</sup> *School of Astronomy and Space Science, Nanjing University, Nanjing, 210093, China*

<sup>4</sup> *Key Laboratory of Modern Astronomy and Astrophysics at Nanjing University, Ministry of Education, Nanjing 210093, China*

<sup>5</sup> *Department of Astronomy, University of Massachusetts, Amherst, MA, 01003, USA*

<sup>6</sup> *Astronomy Department, University of Washington, Seattle, WA, 98195, USA*

<sup>7</sup> *Max Planck Institute for Astronomy, Königstuhl 17, D-69117 Heidelberg, Germany*

*E-mail: hdong@iaa.es*

## ABSTRACT

We map the dust distribution in the central 180'' ( $\sim 680$  pc) region of the M31 bulge, based on *HST* WFC3 and ACS observations in ten bands from near-ultraviolet (2700 Å) to near-infrared (1.5  $\mu$ m). This large wavelength coverage gives us great leverage to detect not only dense dusty clumps, but also diffuse dusty molecular gas. We fit a pixel-by-pixel spectral energy distributions to construct a high-dynamic-range extinction map with unparalleled angular resolution ( $\sim 0.5''$ , i.e.,  $\sim 2$  pc) and sensitivity (the extinction uncertainty,  $\delta A_V \sim 0.05$ ). In particular, the data allow to directly fit the fractions of starlight obscured by individual dusty clumps, and hence their radial distances in the bulge. Most of these clumps seem to be located in a thin plane, which is tilted with respect to the M31 disk and appears face-on. We convert the extinction map into a dust mass surface density map and compare it with that derived from the dust emission as observed by *Herschel*. The dust masses in these two maps are consistent with each other, except in the low-extinction regions, where the mass inferred from the extinction tends to be underestimated. Further, we use simulations to show that our method can be used to measure the masses of dusty clumps in Virgo cluster early-type galaxies to an accuracy within a factor of  $\sim 2$ .

## 1. Introduction

Dust is an important ingredient for star formation, is often released into the interstellar medium (ISM) at the end of stars’ lives, absorbs/scatters light, and radiates significantly from millimeter to infrared. Therefore, accurately mapping the dust in the Universe is critical to correcting for the foreground extinction, measuring the star formation rate, and in turn understanding the evolution of galaxies. Radio observations are a widely used tool to trace various molecules, from which one may infer the dust, assuming a dust-to-gas mass ratio. Because molecular hydrogen ( $\text{H}_2$ ) is notoriously difficult to detect, carbon monoxide molecule (CO) is typically used to infer the mass of molecular clouds. Single-dish radio observations with the high sensitivity needed to detect diffuse molecular clouds of relatively low density, however, often suffer from poor angular resolution at extragalactic distances. Interferometry provides high angular resolution, but typically lacks the sensitivity to detect anything beyond dense, giant molecular cloud cores. In addition, the relationship between CO intensity and  $\text{H}_2$  mass in different environments is also poorly understood (e.g., Bolatto et al. 2013; Sandstrom et al. 2013). Alternatively, thermal far-infrared (FIR) observations can be used to directly detect radiation from dust. However, the angular resolutions of such observatories are poor (even with *Herschel*,  $\geq 6''$ ). Both emissivity and temperature distributions of dust are poorly known in many circumstances. As a result, the inferred ISM mass can be greatly uncertain (Shetty et al. 2009a, 2009b).

Fortunately, dust can be detected through its extinction against background starlight. In the Milky Way and Magellanic Clouds, the hydrogen column densities of molecular clouds have been statistically measured from the near-infrared (NIR) colors of background stars (Lombardi 2009; Dobashi et al. 2008, 2009, and references therein). Compared to the radio and far-infrared observations, this method can reach unparalleled angular resolution and sensitivity because of the availability of high-quality NIR source catalogues, such as 2MASS (Skrutskie et al. 2006). Now the method can be applied to galaxies beyond the Milky Way and Magellanic Clouds, e.g., the M31 disk (Dalcanton et al. 2015), when starlight can be resolved into individual stars and/or their colors can be utilized (e.g., Crockett et al. 2011). With modern observations in the wavelength range from IR to ultraviolet (UV) (e.g., from the Hubble Space Telescope, *HST*), one can, in principle, map the interstellar dust at sub-arcsecond resolutions and over a broad dynamic range.

The interpretation of extinction mapping depends on the line-of-sight location of dusty clouds relative to the stellar light distribution. Only the starlight emitted in regions behind the cloud would suffer from extinction and reddening. Thus, without accounting for this effect (i.e., simply assuming that the cloud is in the foreground), one would underestimate the dust column density and mass (Calzetti et al. 1994). For example, Kreckel et al. (2013)

find that in eight nearby galaxies, the dust mass derived from the stellar continuum (without taking into account the partial extinction) is systematically less than that estimated from the FIR emission from *Herschel* observations. Therefore, determining the obscured fraction of the starlight is a key for a successful use of the extinction method.

The work presented here provides a test of the method developed in Dong et al. (2014, 2015) to address the above problem, using multi-wavelength *HST* data of the M31 bulge. The basic idea is that the fraction of the starlight arising from beyond an obscuring cloud can be measured together with its extinction as a function of wavelength. Therefore, we can use a pixel-by-pixel spectral energy distribution (SED) fitting to derive an extinction map, and subsequently construct a high-resolution dust mass surface density map with a large dynamic range, assuming a dust mass to  $A_V$  ratio. The inferred obscured fraction of starlight can be converted to the radial location of the cloud, if the intrinsic starlight distribution and a screen geometry can be reasonably modelled (see §3). Specifically, we utilize ten images taken by the *HST* Wide Field Camera 3 (WFC3) and Advanced Camera for Surveys (ACS) cameras (listed in Table 1) from the near-UV (2700 Å) to near-IR (1.5  $\mu\text{m}$ ). The high angular resolution (Full Width Half Maximum, FWHM,  $\leq 0.15''$ ,  $\sim 0.6$  pc) of this set of images, combined with the proximity of M31 enables us to resolve dense dusty clumps (Bergin & Tafalla 2007). As a result, the spatial variation of extinction, due to the clumpy effect of these dusty clumps in individual resolution elements, should be largely reduced. The derived surface density map can also be compared with that produced from the *Herschel* observations to examine the reliability of our method.

During the past decade, the interstellar medium in M31, the closest external massive spiral ( $\sim 780$  kpc, McConnachie et al. 2005), has been extensively mapped with various instruments at various bands, such as the Westerbork Synthesis Radio Telescope array for the H I 21 cm emission line (Braun et al. 2009), IRAM 30 m telescope for  $^{12}\text{CO}$  (Nieten et al. 2006), *Spitzer* Space Telescope at mid-IR (3 to 160  $\mu\text{m}$ , Barmby et al. 2006; Gordon et al. 2006) and *Herschel* Space Telescope at FIR (100-500  $\mu\text{m}$ , Fritz et al. 2012; Smith et al. 2012) for dust. Much of the atom or molecular gas is found in so-called the 10 kpc star-forming ring. There are moderate amounts of ionized and molecular gas, as well as dust in the circumnuclear region (CNR) of M31 (Braun et al. 2009; Nieten et al. 2006). For example, based on *Spitzer*/IRAC observations, Block et al. (2006) identify a ring-like dusty structure with an extent of 1 kpc ( $\sim 260''$ ) in the *Spitzer*/IRAC observations, which is part of spiral-like patterns, perviously known as the ‘nuclear spiral’ (Jacoby et al. 1985). Through SED fitting of *Spitzer*/MIPS data (24-160  $\mu\text{m}$ ), Li, Wang & Wakker (2009) report  $\sim 9 \times 10^3 M_\odot$  dust within this nuclear spiral. Groves et al. (2012) give a total dust mass,  $\sim 1.5 \times 10^5 M_\odot$ , within the central 1 kpc of the M31 bulge, through analyzing recent *Herschel* observations. With very deep observations of CO(1-0) and CO(2-1) taken by the IRAM-30m

telescope, Melchior & Combes (2013) give a lower limit of  $4.2 \times 10^4 M_{\odot}$  molecular gas within the central  $30''$  ( $\sim 100$  pc) of the M31 bulge.

Both the content and the morphology of the dusty material in the CNR of M31 are of great interest to the understanding of its origin and interplay with the nuclear environment. Block et al. (2006) notice that both the 1 kpc dusty ring and the well-known 10 kpc star forming ring (Gordon et al. 2006, and references therein) are off-center with respect to M31\*, the supermassive black hole, a phenomenon reminiscent of that observed in the Cartwheel galaxy. These rings are suggested to be the result of a head-on collision between M31 and a satellite galaxy, presumably the nearby M32, roughly 200 Myr ago, which triggered a density wave propagating through the M31 disk. Furthermore, Melchior & Combes (2011) find that several dusty clumps in the northwest of the M31 bulge show distinct velocity components, which may represent the 1 kpc dusty ring and its distortion, due to the putative collision. Melchior & Combes (2013) also suggest that the extinction produced by the 1 kpc dusty ring and its distortion are needed to explain the position-angle distribution of planetary nebulae observed in the central  $200''$  radius of M31. However, without knowing the actual spatial locations of the individual dusty clumps, one cannot be confident about their overall structure and the origin.

The rest of the paper is organized as follows. We describe the observations and data reduction in § 2. We present our pixel-by-pixel SED fitting method, detailed analysis steps and the results in § 3. We discuss the implications of our results in § 4 and give a summary of the work in § 5.

## 2. Data

### 2.1. *HST* multi-band dataset

Detailed description about the *HST* multi-band images are given in Dong et al. (2014, 2015). Here, we briefly describe the data and major reduction steps, as well as an adaptive smoothing procedure performed on the images.

Our images were taken in ten bands. Six of them are from the Panchromatic Hubble Andromeda Treasury program (PHAT, Dalcanton et al. 2012; Williams et al. 2014), including F275W (2704 Å), F336W (3355 Å), F475W (4747 Å), F814W (8057 Å), F110W (1.1  $\mu\text{m}$ ) and F160W (1.5  $\mu\text{m}$ ). The other four images are from Program GO-12174 (Li et al. 2016, in preparation), including F390M (3897 Å), F547M (5447 Å), F665N (6656 Å) and Program 10006, Program 10760 and Program 11833 (Williams et al. 2005) on F435W (4319 Å). The F547M band is approximately the traditional Johnson *V* band, because they have

similar central wavelengths. The images in these ten bands have different fields-of-view.

We performed the basic calibration steps, such as identifying bad pixels, dark subtraction and flat-fielding correction with `CALWFC3` and `CALACS` in `PyRAF`<sup>1</sup>. We used the `Astrodrizzle` to merge dithered exposures for each pointing and filter. We corrected for the relative astrometry and bias offset among pointings of individual filters with the method developed by Dong et al. (2011). These pointings were then aligned to the absolute astrometry defined by bright objects found in the 2MASS catalog (Skrutskie et al. 2006). We merged the images of different pointings into the  $250'' \times 250''$  ( $950 \text{ pc} \times 950 \text{ pc}$ ) mosaic for each of the ten bands. We converted the image units from the count rate (electron/s) to intensity ( $\text{erg cm}^{-2} \text{ s}^{-1} \text{ \AA}^{-1}$ ) by multiplying the mosaics with the ‘PHOTFLAM’ values listed in Table 1. The intensity uncertainty of each pixel ( $\sigma_n$ , where the subscript indicates the filter number) was derived in Dong et al. (2015) and consists of two parts: statistic and systematic errors. The statistic error, the intensity variation among pixels, was empirically derived within the mosaic, while the systematic uncertainty was from ‘PHOTFLAM’ (Table 1; see Dong et al. 2015 for details). Foreground Galactic extinction ( $E(B-V)=0.062$ , i.e.,  $A_V=0.17$ , Schlafly & Finkbeiner 2011) was corrected for the intensity in each band. We then employed `PSFMATCH` in `PyRAF` to construct PSF kernels and convolved them with mosaics one-by-one to the resolution of the F160W band. We also rebinned the mosaics to the common pixel size ( $0.13''$ ) of the WFC3/IR.

We adaptively smoothed the mosaics to make sure that each resolution element has at least  $10^5 M_\odot$ , in order to minimize the systematic errors on age and mass due to stochastic fluctuations in the stellar evolutionary synthesis (Fouesneau & Lançon 2010). The mass-to-light ratio ( $M/L$ ) of the F160W band is the least sensitive to the extinction, stellar age and metallicity in our dataset. We thus estimated the stellar mass surface density distribution from the intensity in the band using a conversion  $M/L_{F160W}=1.8$ , where  $M$  and  $L_{F160W}$  are in units of  $M_\odot$  and  $L_\odot$ , appropriate for a 10 Gyr old stellar population with solar metallicity. We employed a smoothing square box<sup>2</sup> centered on each pixel and adaptively scaled to enclose a total of at least  $10^5 M_\odot$ . The average intensity and its variance are measured within this box for each of the ten *HST* filters. These measurements are used for the SED-fitting of this pixel. The angular resolution of our extinction map is thus determined by the size of the box, which generally increases with the galactocentric distance. But the box sizes for 93% of the pixels are still  $<7$  pixel, or  $0.9''$ . On average, the angular resolution of our final

---

<sup>1</sup>‘PyRAF’ and ‘PyRAF’ are the product of the Space Telescope Science Institute, which is operated by AURA for NASA.

<sup>2</sup>In principle, one may employ circular smoothing kernels, such as Gaussian or circular top-hat. We have adopted boxy kernel for simplicity. We find no artifacts due to our choice in the final extinction map.

extinction map is  $\sim 0.5''$  or 1.9 pc at the distance of M31.

The final images in the F336W, F435W, F547M and F160W bands are presented in Fig. 1. We can clearly see the dusty clumps in the CNR as dark fuzzy filaments in the UV band (F336W), which appear weak in the optical (F435W/F547M) images and finally disappear in the IR band (F160W). The F547M image from Program GO-12174 has only one pointing and the smallest sky coverage. The observation in the F435W band covers most of the field-of-view, except for the southwest of the M31 bulge. When we perform the SED fitting in §3, we use all available filters. All pixels over the field-of-view of the F547M image have ten data points (except for the ‘death star’ regions of the WFC3/IR and the WFC3/UVIS CCD gap). However, the bottom-right (southwest) corner is covered by only six PHAT filters.

## 2.2. FIR Dust Mass Surface Density Map

We updated the FIR dust mass surface density map of Groves et al. (2012) to be contrasted with our map derived from the extinction. New calibration files were applied and the absorption cross-section was updated to the value given in Draine & Hensley (2013). A  $\chi^2$  minimization SED fitting with a modified blackbody was employed on three *Herschel* bands: PACS 100  $\mu\text{m}$ , 160  $\mu\text{m}$  and SPIRE 250  $\mu\text{m}$  to measure the dust temperature and mass, as well as the emissivity index,  $\beta$ . The pixel size of this surface density map is  $6''$ , while the FWHM is limited by the SPIRE 250  $\mu\text{m}$  camera,  $18''$ .

We first compare the map of Groves et al. (2012) with other three recent ones: two from Draine et al. (2014) and one from Viaene et al. (2014). Draine et al. (2014) fitted a physical dust SED model to the same *Herschel* dataset and *Spitzer* observations from 3 to 500  $\mu\text{m}$ . They provided two versions of the dust mass surface density map, with or without *Spitzer*/MIPS 160  $\mu\text{m}$  and *Herschel*/SPIRE 500  $\mu\text{m}$  data included in the fit. The former map has a higher angular resolution ( $25''$ ), while the latter one, though with poorer resolution ( $39''$ ), allows for better constraint on the dust with temperature below 20  $K$ . Viaene et al. (2014) modelled the far-UV to FIR SED constructed with *GALEX*, SDSS, WISE, *Spitzer* and *Herschel* observations. The size of their fitting element is  $36'' \times 36''$ . Fig. 2 compares the enclosed dust mass as a function of galactocentric radius derived from these four maps. The two curves from the maps of Draine et al. (2014) are very similar because the M31 bulge is dominated by hot dust ( $\sim 35 K$ , Draine et al. 2014; Groves et al. 2012). The dust mass surface densities of Draine et al. (2014) and Groves et al. (2012) differ by as much as 100% in the central  $50''$  radius, but converge beyond that. Therefore, the total mass within the central  $180''$  from the map of Draine et al. (2014) is only larger than that of Groves et al. (2012) by 18%.



The dust mass derived by Viaene et al. (2014) is smaller than those of Draine et al. (2014) and Groves et al. (2012); the total mass within the central 180'' from the map of Viaene et al. (2014) is only 65% of that of Groves et al. (2012). We suspect that this shortfall is a result of the shallower observations or different calibration procedures used by Viaene et al. (2014). Based on these comparisons, we suggest that the uncertainty in the FIR dust mass surface density map is  $\sim 50\%$ .

### 3. Analysis and Results

#### 3.1. Method

We utilize a pixel-by-pixel SED fitting method to map the extinction distribution in the CNR of M31 with the *HST* mosaic images described above. Considering the relatively low column density and small filling factors of dusty clumps in the M31 bulge (Melchior & Combes 2011, and Fig. 1), we assume that their sizes are much smaller than that of our covered CNR field and that they are thin and are not overlapped with each other along any line of sight. Under this assumption, the starlight behind a dusty clump is attenuated, while its foreground does not.

Dong et al. (2015) focused on constraining the stellar populations, using a  $\chi^2$  minimization. The  $\chi^2$  for each pixel is defined as the sum of the deviations between the observed flux  $I_n$  (in the  $n^{th}$  filter) and the theoretical flux  $S_n$  of a ‘Starburst99’ stellar population synthesis model (Vázquez & Leitherer 2005) with certain age and metallicity:

$$\chi^2 = \sum_{n=1}^N \frac{\langle I_n - [(1-f) + f \times 10^{-0.4 \times \frac{A_n}{A_{F547M}} A_{F547M}}] S_n \mathfrak{N} \rangle^2}{\sigma_n^2} \quad (1)$$

where  $0 \leq f \leq 1$  is the fraction of the starlight that is subject to the extinction,  $A_{F547M}$  is the absolute extinction in the F547M band,  $A_n/A_{F547M}$  is the relative extinction,  $\sigma_n$  is the uncertainty of  $I_n$  (see §2) and  $\mathfrak{N}$  is a normalization. The sum is over all of the filters that cover the pixel. We adopt the average extinction curve,  $A_n/A_{F547M}$ , of five well-defined dense dusty clumps in the CNR of M31, as obtained by Dong et al. (2014), given in Table 1.  $A_{F547M}$  is not constrained to be positive, so that we can derive the uncertainty of  $A_{F547M}$  of our SED fitting from the  $A_{F547M}$  distribution later.

To break the notorious extinction-age-metallicity degeneracy, we determined  $S_n$  independently. As detailed in Dong et al. (2015), we first performed the SED fitting for several regions of low-extinction in the southeast portion of the M31 bulge, leading to a characterization of the radial distribution of the stellar age and metallicity, out to a projected major-axis

radius of  $180''$  (see Fig. 1). We used two single-epoch populations and fit the observed magnitudes from the ten bands with six free parameters: the ages and metallicities of the two populations, the mass fraction of the young stellar population and the total mass. One starburst represents the well-established old stellar population ( $\sim 12$  Gyr), while the other has an age of a few hundred Myr (0.3–1 Gyr). Both stellar populations are metal-rich. The young stellar population contributes  $\sim 1\%$  of the total stellar mass in the inner bulge of M31. This radial SED distribution was then used to calculate  $S_n$  for pixels in the individual isophotes, which nicely follow an elliptical shape. The pixels outside the outermost isophote, corresponding to the outermost radius of the SED distribution measurement, were not used in the subsequent fit.

The fit is to obtain  $A_{F547M}$  and  $f$ , as well as the normalization  $\aleph$ . Compared to previous work (Melchior et al. 2000; Melchior & Combes 2013),  $f$  is a new parameter and is anti-correlated with  $A_{F547M}$ . Because of this anti-correlation, the uncertainties of these two parameters can be large for any pixel with the ratio of the observed to intrinsic intensities smaller than 1 by less than two-sigma in the near-UV and optical bands (see Dong et al. 2014 for more details about the intrinsic intensities and the sigma), due to either a low  $A_{F547M}$  or a small fraction of obscured starlight  $f$ . To overcome this coupling, we assume that  $f$  changes smoothly across the field (e.g., dusty gas forms a coherent structure in the bulge, the consistency of which is checked later). Specifically, we smooth the  $f$  map from the initial  $\chi^2$  fit with a  $11 \times 11$  pixel box median filter to reduce the pixel-by-pixel fluctuation and to increase the reliability of the  $f$  estimation for the pixels with either low extinction or a small fraction of obscured starlight.

After  $f$  is derived and fixed, we rerun the  $\chi^2$  fitting to determine  $A_{F547M}$  and  $\aleph$  for each pixel. The peak of reduced  $\chi^2$  is around 0.46 for all pixels and is less than 2 for 81% of the individual pixels, indicating an acceptable fit.

### 3.2. Extinction Map

Our final extinction map ( $A_{F547M}$ ) is presented in Fig. 3 with color bar, in which bright regions represent dusty clumps with high extinction. Overall, the extinction map is very smooth and we do not see any artifacts introduced by the different numbers of bands used in the SED fitting across the map.

Fig. 4 presents the distribution of  $A_{F547M}$  for the fitted pixels (black solid line). The peak of the distribution can well be approximated with a Gaussian. Its width is chiefly due to the photometric uncertainty, as well as variation in the extinction by diffuse dust.



Its mean extinction value may be characterized by the peak position of the Gaussian at 0.014 mag and the uncertainty of our extinction map ( $\delta A_{F547M}$ ) by the standard deviation, 0.054 mag. The tail on the negative side of the extinction distribution is primarily due to the presence of globular star clusters and foreground Galactic halo stars, which are bluer than the predominant low-mass stars in the M31 bulge. The tail on the positive side primarily traces dense dusty clumps in the CNR of M31. For comparison, Fig. 4 also shows the distribution of  $A_{F547M}$  obtained with fixed  $f=1$  (blue solid line), which assumes that all dust extinction is in the foreground of the M31 bulge. We can see that  $A_{F547M}$  in this alternative distribution is underestimated by a factor of 2-3, compared with that allowing for spatially-varying  $f$ .

The filling factor of the dusty clumps in the M31 bulge is very low; only 7% of the pixels in our field-of-view have  $A_{F547M}$  larger than  $3\delta A_{F547M}$ . Especially in the central  $10''$ , the extinction is small ( $A_{F547M} < \delta A_{F547M}$  for 94% pixels), which indicates a paucity of dust in the nucleus of M31, consistent with previous works (Li, Wang & Wakker 2009; Melchior & Combes 2011).

### 3.3. $f$ Map

Fig. 5 shows the spatial distribution of  $f$  for the pixels with  $A_{F547M} > 3\delta A_{F547M}$ , which have small uncertainty in  $f$ . For most of these pixels, the ratio of the observed to intrinsic intensities is smaller than 1 by more than two-sigma in the near-UV and optical bands and did not experience the smoothing step of  $f$  (§3.1). Table 2 includes the mean and standard deviation of  $f$  for such pixels in ten selected dusty clumps shown in Fig. 5. The dusty clumps ‘A’ to ‘E’ are used in Dong et al. (2014) to constrain the extinction curve in the M31 bulge. The fractions of obscured starlight of these dusty clumps from Dong et al. (2014) and this work are consistent with each other within twice the measurement uncertainties.

We follow the steps in Appendix C of Dong et al. (2014) to translate the fraction of obscured starlight into the line-of-sight offsets of the dusty clumps from M31\*. This translation assumes a two-dimensional Sersic profile for the the M31 bulge with a fitted index of 2.2 (Li et al. 2016, in preparation; see also Kormendy & Bender 1999; Courteau et al. 2011). Table 2 includes the derived line-of-sight offsets and the projected off-center distances of the clumps.

### 3.4. Dust Mass

We convert our extinction map to the dust mass surface density map ( $\sum M_{de}$  in units of  $M_{\odot}/\text{pixel}$ ) by choosing the ratio of  $\frac{A_{F547M}}{M_{dust}}$ . This ratio assumes a size distribution of dust grains, which is characterized by the total to selective extinction ratio,  $R_V$ . Dong et al. (2014) shows that  $R_V=2.4-2.5$  in the M31 bulge is similar to  $R_V \sim 2.7$  in the Small Magellanic Cloud, but much smaller than the canonical value of  $\sim 3.1$  in the Milky Way. Therefore, we adopt  $\frac{A_{F547M}}{M_{dust}}=3.8$  ( $\text{mag } M_{\odot}^{-1} \text{ pc}^2$ ), typical of the Small Magellanic Cloud (Draine & Li 2007; Draine et al. 2014). The total dust mass covered by the pixels with  $A_{F547M} > \delta A_{F547M}$  in the central  $180''$  (i.e., 680 pc) region is  $\sim 1.1 \times 10^4 M_{\odot}$ . Table 3 gives the dust mass of the ten clumps shown in Fig. 5.

We compare our dust mass surface density map with that ( $\sum M_{dH}$ ) derived from the *Herschel* FIR observations described in §2.2. Because the resolution of the latter is much poorer, we convolve our map with the PSF of *Herschel* SPIRE 250  $\mu\text{m}$  and then rebin it to  $6''$   $\text{pixel}^{-1}$ . Fig. 6 shows that the two maps are broadly similar in morphology. However, there are also marked differences between the two maps. For example, the dusty clump southeast of the M31 bulge, as outlined by the cyan ellipse in Fig. 6, is visible only in far-IR (see §4 for more discussion about this clump). Fig. 7(a) gives a pixel by pixel comparison of  $\sum M_{de}$  and  $\sum M_{dH}$ . At pixels of low extinction, especially those below its uncertainty ( $\delta A_{F547M}$ ),  $\sum M_{dH}$  is always greater than  $\sum M_{de}$ ; a good example of this trend is the dusty clump southeast of the M31 bulge mentioned above. The ratio between  $\sum M_{dH}$  and  $\sum M_{de}$  decreases with the increase of  $\sum M_{de}$ . At pixels with  $\sum M_{de}$  above twice the uncertainty, the ratio is close to 1. Fig. 7(b) provides a similar comparison, but for a fixed  $f=1$ .

We also measure the dust-to-gas mass ratio in the M31 bulge. The largest dusty clump in our field-of-view is D395A/393/384 (green ellipse in Fig. 3),  $1.3'$  ( $\sim 300$  pc) northeast of M31\*. Melchior & Combes (2011) give  $I_{CO(1-0)}=0.72 \pm 0.03$  K km s $^{-1}$  (with a  $24''$  beam size) for this clump, i.e.,  $(9.8 \pm 0.4) \times 10^3 M_{\odot}$  molecular gas, assuming the conversion factor between the CO emission and  $H_2$  mass given in Leroy et al. (2011). In the same region, the H I mass is  $1.4 \times 10^4 M_{\odot}$ , according to the map of Braun et al. (2009). Our surface density map of dust mass gives  $706 \pm 219 M_{\odot}$ , which is consistent with the value,  $603 M_{\odot}$ , from the FIR map given in §2.2. Therefore, we derive a dust-to-gas mass ratio of  $0.03 \pm 0.009$ , consistent with the value of 0.026 given in Draine et al. (2014) for the entire center of M31.

## 4. Discussion

Here, we explore the structure of the dusty materials in the central region of M31 using our newly estimated locations of the dusty clumps in §4.1 and discuss the reliability of the method in mapping the dust in §4.2.

We first compare our results with other observations. The overall structure of our extinction map is qualitatively similar to that of Melchior et al. (2000) (their Figure 1; though at  $1''$  resolution), which is derived from a ground-based  $B$ -band image. The high extinction regions show filament structures around M31\* and trace the *Spitzer*/IRAC  $8\ \mu\text{m}$  emission very well (Fig. 8a), indicating that the hot dust is indeed associated with the dusty clumps. As noted by Melchior & Combes (2013), however, one clump southeast of M31\* (cyan ellipse in Fig. 8a) has strong  $8\ \mu\text{m}$  emission, but does not show up in the extinction map, indicating that it is located at the far side of the M31 bulge. Fig. 8b shows that the  $\text{H}\alpha + [\text{N II}]$  emission, which will be studied in details in an upcoming paper by Li et al. (2016, in preparation).

### 4.1. Nuclear Spiral Structure

Which dusty clumps are associated with the nuclear spiral of M31? Most of the dusty clumps shown in Fig. 5 have the radial (line-of-sight) offsets from M31\* smaller than 50 pc, which indicates that they are indeed within the bulge. This provides a natural explanation of their associations with the ionized gas ( $\text{H}\alpha + [\text{N II}]$ ), which is thought to be heated by hot stars concentrated toward the nucleus (e.g., post-AGBs; Binette et al. 1994) and by type-Ia supernova shocks in the bulge (Jacoby et al. 1985). In contrast, Clump D, and the clump enclosed by the cyan ellipse in Fig. 8a do not show significant  $\text{H}\alpha + [\text{N II}]$  emission. Therefore, these two dusty clumps likely have large off-nucleus radial distances.

Because of their close spatial distribution, these ten dusty clumps may belong to a coherent disk-like structure, only slightly inclined with respect to our line of sight. The clumps to the northeast, such as ‘B’, ‘E’ and ‘F’, are slightly beyond the nucleus (but still  $< 25$  pc). These dusty clumps extend northwest to ‘D395A/393/384’ (‘J’ in Fig. 5), which becomes in front of the bulge. On the other hand, the dusty clumps in the south, ‘H’ and ‘I’ are behind M31\*.

This structure does not align with the galactic disk of M31, which has an inclination angle of  $77^\circ$ . Figure 9 compares the  $f$  values for the individual dusty clumps in Table 2 with what would be expected if they were in the galactic disk plane. This expectation is based on the starlight model of M31, in which the stellar bulge is a triaxial ellipsoid and

that the M31 disk is a thin plane. The model  $f$  values are then derived from their projected off-nucleus distances, following the procedure detailed in Appendix C of Dong et al. (2014). Figure 9, shows that the range of the  $f$  values (all around 0.5) is much smaller than expected from the galactic disk model. Therefore, the nuclear dusty structure is tilted off from the galactic disk and is consistent with a nearly face on configuration.

The misalignment of the nuclear dusty structure and the galactic disk indicates violent activities which happened in the M31 bulge in the recent past. The dusty clumps in the bulge of spiral galaxies can originate from the disk and be transported into the bulge through the torque of a bar (Kormendy & Kennicutt 2004). Therefore, the dusty clumps are supposed to inherit the dynamical information of the galactic disk. External forces are needed to disturb the dusty clumps from their original orbit. The head-on collision between M31 and M32 suggested by Block et al. (2006) and Melchior & Combes (2011) could play such a role in shaping the molecular clouds in the CNR of M31.

#### 4.2. The Reliability of Tracing Dust with Extinction

Kreckel et al. (2013) discuss the reliability and feasibility of mapping dust with extinction estimated from the Balmer decrement and stellar continuum shape for eight nearby galaxies. From the intensity ratio of  $H\alpha/H\beta$  and the SED-fitting of the observed stellar continuum in the wavelength range of 3700–7000 Å, they produce two apparent dust reddening maps with resolutions of 20-100 pc for these galaxies. However, the extinction derived from the stellar continuum shows no linear correlation with the dust mass from the *Herschel* FIR data, which is considered as a standard. This nonlinearity is attributed to the mixed distribution between the dust and the light from stars with a board range of ages. In contrast, a linear correlation is found between the dust mass and the extinction derived from the line ratio, which can be explained by a close association of the dense dusty gas with recent/ongoing star-forming regions.

Unlike Kreckel et al. (2013), we find a linear relationship between the dust mass derived from the extinction and dust emission in the high extinction regions in the CNR of M31. At  $A_{F547M} > 3\delta A_{F547M}$ ,  $\sum M_{dH} = (1.06 \pm 0.07) \times \sum M_{de} + (0.008 \pm 0.004)$ . In Fig. 10, we show good agreement between the dust mass of the dense dusty clumps derived from our method with spatially-varying  $f$  and for the *Herschel* dat. The median and the standard variation of the ratios between the two masses are  $0.99 \pm 0.34$ . Instead, for fixed  $f=1$ , the median and the standard deviation of the ratios would be only  $0.28 \pm 0.11$ .

This good consistency is due to several advantages in our work: 1) Our angular resolution

reaches  $\sim 2$  pc ( $0.5''$ ), better than that of Kreckel et al. (2013) by more than an order of magnitude. In the CNR of M31, even the cores of small dusty clumps seem to be reasonably well resolved; 2) The relative distribution between starlight and extinction in the M31 bulge is much simpler than in the irregular and spiral galaxies in Kreckel et al. (2013); 3) Most importantly, in our SED-fitting we have introduced the parameter  $f$ , which allows us to quantitatively separate the unobscured foreground starlight from the background.

However, when moving into the low-extinction regions, especially for  $A_{F547M} < \delta A_{F547M}$ , we seriously underestimate the amount of dust (see Fig. 7). There are several reasons why the extinction can not reproduce the dust mass: 1) The dusty clumps, such as the one in the southeast of M31\* (the cyan ellipse in Fig. 6), are far behind the M31 bulge and hence the fractions of obscured starlight are so low that the dusty clumps have little signal even in the UV images. This effect is demonstrated in Fig.11, which shows the ratio of the observed to intrinsic F275W intensities as a function of  $f$  for a molecular cloud with different  $A_{F547M}$ . We can see that for  $f < 0.15$ , even a cloud with  $A_{F547M} = 2$  can lead to 14% extinction, which is comparable to the photometric uncertainty in this band; and 2) In the low-extinction regions, the diffuse dust may pervade the M31 bulge and may be well mixed with stars. As a result, they also leave very few signals in the observed UV images. From the *Herschel* image, the median dust surface density in the M31 bulge is  $0.036 \text{ M}_{\odot}/\text{pc}^2$ , which corresponds to  $A_{F547M} \sim 0.1$ . For uniformly distributed diffuse dust, we only expect that it reduces the intensity at the F275W band by 12%, also smaller than the photometric uncertainty. Accurately determining the diffuse dust needs detailed radiation transfer modeling.

In the low-extinction region, the intensity ratio of  $\text{H}\alpha/\text{H}\beta$  also underestimates the dust mass. For example, in the eight galaxies studied in Kreckel et al. (2013), the ratio between the apparent extinction from the stellar continuum and the  $\text{H}\alpha/\text{H}\beta$  is less than one in high extinction regions and becomes greater than one in low extinction regions. In this latter case, most of the hydrogen recombination line emission may arise from the scattered light, which suffers from less extinction than the stellar continuum.

We conduct simulations to test how our method may be applied to relatively distant galaxies. We artificially put M31 at a distance comparable to those of the Virgo cluster galaxies and re-measure the masses of the dusty clumps in Fig. 5. We assume the distance of the Virgo cluster to be 16.5 Mpc (Tonry et al. 2001), correspondingly downgrade our *HST* images by a factor of 21, and redo our measurement as in §3. The measured dust masses are given in Table 3 and are compared with those from the *Herschel* observations in Fig. 10. The ratio of the dusty masses from the extinction and from the far-IR emission is  $1.19 \pm 0.9$ . Although the uncertainty is larger than that of M31, due to the reduced physical resolution,

the median value suggests that our method can still give an reasonably accurate estimate of the dust mass for molecular clouds in distant galaxies.

Therefore, extinction measurements could be used to map dust in remote galaxies, when two conditions are satisfied: 1) The sizes of molecular clouds are discrete and compact, compared to the extent of a galactic spheroid, such as dust lanes in giant elliptical galaxies, where a screen assumption can reasonably be made; 2) The fraction of the obscured starlight,  $f$ , should be large enough that the extinction can be accurately measured. In such case, we can then simultaneously determine both the fraction of obscured starlight and the amount of dust.

## 5. Summary

We have mapped the dusty clumps in the circumnuclear region of M31 via their extinction of background starlight in multiwavelength bands. Thanks to the high angular resolution and sensitivity of the WFC3 and ACS data, we have achieved an unparalleled  $\sim 0.5''$  (2 pc) resolution in the final extinction map. Because our dataset spans from near-ultraviolet to near-infrared, the map has a large dynamic range and an uncertainty of  $\delta A_{F547M} = 0.055$  mag.

The main innovation of our work is the measurement of the fraction of obscured starlight,  $f$ , across the field. With the fraction included in our SED fit for dense dusty clumps, the extinction typically increases significantly by a factor of 2-3, compared to those by simply assuming a foreground screen ( $f=1$ ). We have found that most of the clumps have  $f \sim 0.5$  (line-of-sight offset from M31\*,  $< 50$  pc), indicating that they are indeed in the central region of M31 and represent a coherent structure. Compared to the M31 disk, this structure has a small inclination and seems to be consistent with the inner ring claimed by Melchior & Combes (2011). This geometry agrees with the prediction from the H $\alpha$ -emitting gas observations; the shocked heated gas are associated with the inner side of the structure around M31\*, consistent with the scenario that the ISM in the center of M31 was strongly disturbed in the recent past by, for example, a collision between M31 and M32.

We have converted our extinction map into a surface density map of dust mass. The total dust mass in D395A/393/384, the largest dusty clump in the central  $2'$  of the M31 bulge, is  $\sim 700 M_{\odot}$ . We have also inferred the dust-to-gas mass ratio,  $0.03 \pm 0.009$ , which is consistent with the value given in Draine et al. (2014).

We have compared our surface density map with that from recent *Herschel* far-infrared observations. In the low extinction regions, where our map seriously underestimates the dust mass. In the regions with  $A_{F547M} > 3\delta A_{F547M}$ , however, the dust extinction is consistent



with the amount of dust, as seen in far-infrared emission. Our simulations have further shown that a similar method may be used to detect high extinction clumps in early-type galaxies in the Virgo cluster.

### Acknowledgments

We thank the anonymous referee for a thorough, detailed, and constructive commentary on our manuscript. This work uses observations made with the NASA/ESA Hubble Space Telescope and the data archive at the Space Telescope Science Institute, which is operated by the Association of Universities for Research in Astronomy, Inc. under NASA contract NAS 5-26555. The work is partially supported by NASA via the grant GO-12055 and GO-12174 provided by the Space Telescope Science Institute. The work has also received funding from the European Research Council under the European Union’s Seventh Framework Programme (FP7/2007-2013) / ERC grant agreement n [614922]. H. D. acknowledges the support and hospitality of the Key Laboratory of Modern Astronomy and Astrophysics at Nanjing University during his visit, and would like to thank Bruce Draine, Robert Braun and Sebastien Viaene for providing their dust mass surface density maps and H I map. Z. L. acknowledges support from the Recruitment Program of Global Experts and the National Science Foundation of China through grant 131147.

### REFERENCES

- Barmby, P., Ashby, M. L. N., Bianchi, L., et al. 2006, *ApJ*, 650, L45
- Bergin, E. A., & Tafalla, M. 2007, *ARA&A*, 45, 339
- Binette, L., Magris, C. G., Stasińska, G., & Bruzual, A. G. 1994, *A&A*, 292, 13
- Block, D. L., Bournaud, F., Combes, F., et al. 2006, *Nature*, 443, 832
- Bolatto, A. D., Wolfire, M., & Leroy, A. K. 2013, *ARA&A*, 51, 207
- Braun, R., Thilker, D. A., Walterbos, R. A. M., & Corbelli, E. 2009, *ApJ*, 695, 937
- Calzetti, D., Kinney, A. L., & Storchi-Bergmann, T. 1994, *ApJ*, 429, 582
- Crockett, R. M., Kaviraj, S., Silk, J. I., et al. 2011, *ApJ*, 727, 115
- Courteau, S., Widrow, L. M., McDonald, M., et al. 2011, *ApJ*, 739, 20

- Dalcanton, J. J., Williams, B. F., Lang, D., et al. 2012, *ApJS*, 200, 18
- Dalcanton, J. J., Fouesneau, M., Hogg, D. W., et al. 2015, *ApJ*, 814, 3
- Dobashi, K., Bernard, J.-P., Hughes, A., et al. 2008, *A&A*, 484, 205
- Dobashi, K., Bernard, J.-P., Kawamura, A., et al. 2009, *AJ*, 137, 5099
- Dong, H., Wang, Q. D., Cotera, A., et al. 2011, *MNRAS*, 417, 114
- Dong, H., Li, Z., Wang, Q. D., et al. 2014, *ApJ*, 785, 136
- Dong, H., Li, Z., Wang, Q. D., et al. 2015, *MNRAS*, 451, 4126
- Draine, B. T., & Li, A. 2007, *ApJ*, 657, 810
- Draine, B. T., & Hensley, B. 2013, *ApJ*, 765, 159
- Draine, B. T., Aniano, G., Krause, O., et al. 2014, *ApJ*, 780, 172
- Fouesneau, M., & Lançon, A. 2010, *A&A*, 521, A22
- Fritz, J., Gentile, G., Smith, M. W. L., et al. 2012, *A&A*, 546, A34
- Gordon, K. D., Bailin, J., Engelbracht, C. W., et al. 2006, *ApJ*, 638, L87
- Groves, B., Krause, O., Sandstrom, K., et al. 2012, *MNRAS*, 426, 892
- Jacoby, G. H., Ford, H., & Ciardullo, R. 1985, *ApJ*, 290, 136
- Kreckel, K., Groves, B., Schinnerer, E., et al. 2013, *ApJ*, 771, 62
- Kormendy, J., & Bender, R. 1999, *ApJ*, 522, 772
- Kormendy, J., & Kennicutt, R. C., Jr. 2004, *ARA&A*, 42, 603
- Leroy, A. K., Bolatto, A., Gordon, K., et al. 2011, *ApJ*, 737, 12
- Li, Z., Wang, Q. D., & Wakker, B. P. 2009, *MNRAS*, 397, 148
- Lombardi, M. 2009, *A&A*, 493, 735
- McConnachie, A. W., Irwin, M. J., Ferguson, A. M. N., et al. 2005, *MNRAS*, 356, 979
- Melchior, A.-L., Viallefond, F., Guélin, M., & Neininger, N. 2000, *MNRAS*, 312, L29
- Melchior, A.-L., & Combes, F. 2011, *A&A*, 536, A52

- Melchior, A.-L., & Combes, F. 2013, *A&A*, 549, A27
- Nieten, C., Neininger, N., Guélin, M., et al. 2006, *A&A*, 453, 459
- Sandstrom, K. M., Leroy, A. K., Walter, F., et al. 2013, *ApJ*, 777, 5
- Schlaafly, E. F., & Finkbeiner, D. P. 2011, *ApJ*, 737, 103
- Smith, M. W. L., Eales, S. A., Gomez, H. L., et al. 2012, *ApJ*, 756, 40
- Shetty, R., Kauffmann, J., Schnee, S., & Goodman, A. A. 2009, *ApJ*, 696, 676
- Shetty, R., Kauffmann, J., Schnee, S., Goodman, A. A., & Ercolano, B. 2009, *ApJ*, 696, 2234
- Skrutskie, M. F., Cutri, R. M., Stiening, R., Weinberg, M. D., Schneider, S., Carpenter, J. M., Beichman, C., Capps, R., Chester, T., Elias, J. et al., 2006, *AJ*, 131, 1163S
- Tonry, J. L., Dressler, A., Blakeslee, J. P., et al. 2001, *ApJ*, 546, 681
- Vázquez, G. A., & Leitherer, C. 2005, *ApJ*, 621, 695
- Williams, B. F., Garcia, M. R., Kong, A. K. H., Primini, F. A., & Murray, S. S. 2005, *ApJ*, 620, 723
- Williams, B. F., Lang, D., Dalcanton, J. J., et al. 2014, *ApJS*, 215, 9
- Viaene, S., Fritz, J., Baes, M., et al. 2014, *A&A*, 567, A71

Table 1. *HST* Multi-Wavelength Observations

Filter	Detector	Pivot $\lambda$ ( $\text{\AA}$ )	PHOTFLAM $\text{ergs cm}^{-2} \text{s}^{-1} \text{\AA}^{-1}$	Systematic error of PHOTFLAM <sup>a</sup>	Median of $\sigma/I$ (%) <sup>b</sup>	$A_n/A_{F547M}$ Milky Way <sup>c</sup>	$A_n/A_{F547M}$ M31 bulge <sup>d</sup>
F275W	WFC3 /UVIS	2704	3.3010e-18	3.5%	13.1	1.92	2.80
F336W	WFC3 /UVIS	3355	1.3129e-18	2%	3.7	1.62	1.92
F475W	ACS/WFC	4747	1.8210e-19	2%	4.1	1.16	1.21
F814W	ACS/WFC	8057	7.0332e-20	2%	7.8	0.58	0.61
F110W	WFC3 /IR	11534	1.5274e-20	2%	12.7	0.33	0.46
F160W	WFC3 /IR	15369	1.9276e-20	2%	14.7	0.20	0.43
F390M	WFC3 /UVIS	3897	2.5171e-18	2%	3.1	1.48	1.58
F547M	WFC3 /UVIS	5447	4.6321e-19	2%	4.1	1.0	1.0
F665N	WFC3 /UVIS	6656	1.9943e-18	2%	5.0	0.80	0.73
F435W	ACS/WFC	4318.9	3.1840e-19	2%	3.6	1.30	1.37

Note. — a) The ‘PHOTFLAM’ information is obtained from: [http://www.stsci.edu/hst/wfc3/phot\\_zp\\_lbn](http://www.stsci.edu/hst/wfc3/phot_zp_lbn) (WFC3) and <http://www.stsci.edu/hst/acs/analysis/zeropoints/#tablestart> (ACS). b) ‘I’ and  $\sigma$  are the intensity and uncertainty at individual pixels (in unit of electron  $\text{s}^{-1}$ ). c) The relative extinction  $A_n/A_{F547M}$  for the MW-type dust. d) The average relative extinction  $A_n/A_{F547M}$  of the five dusty clumps in the M31 bulge, derived in Dong et al. (2014).

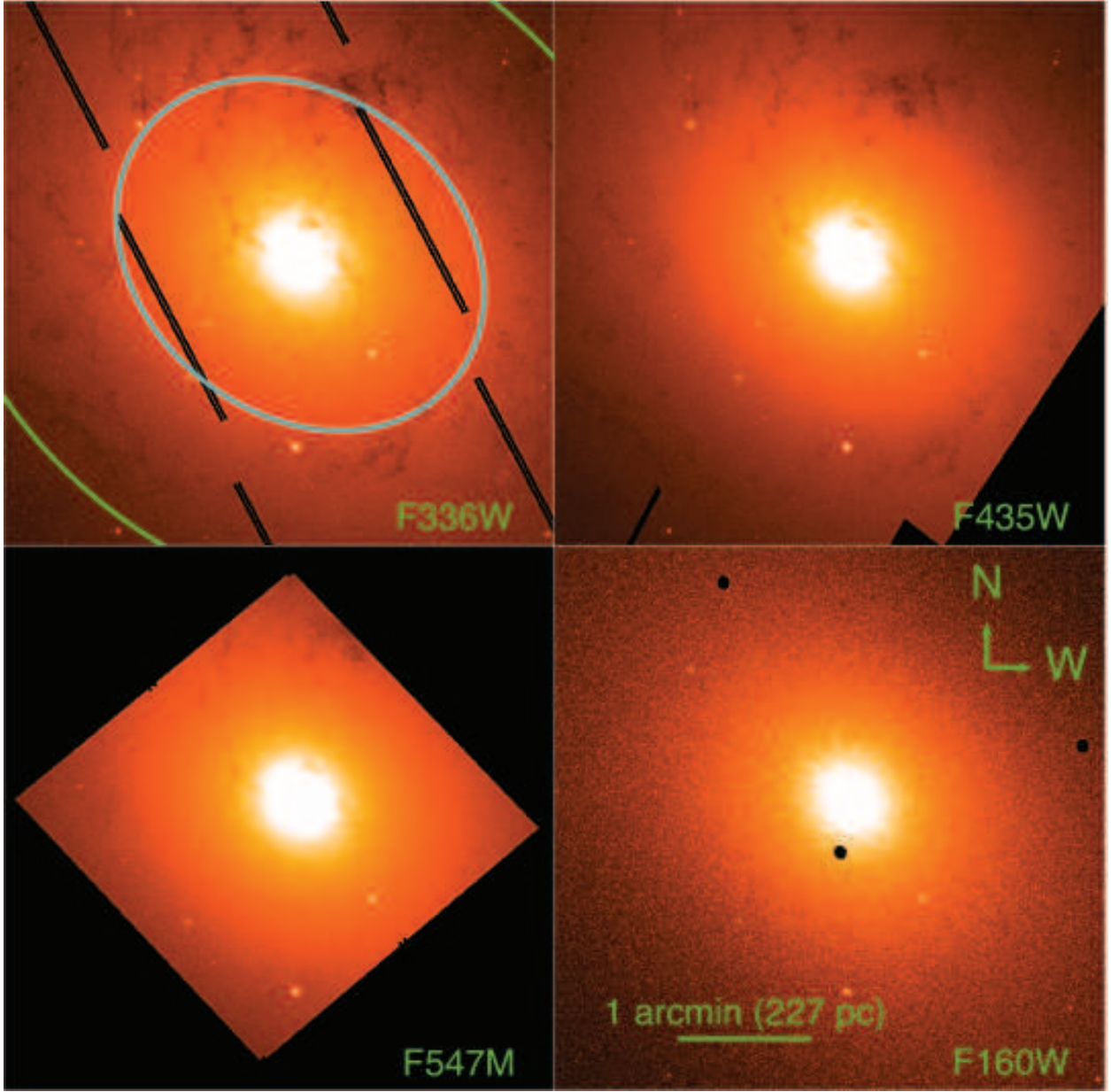


Fig. 1.— The mosaic images of F336W, F435W, F547M and F160W. The dusty clumps in the CNR of M31 can be clearly seen as the dark fuzzy filaments in the UV band (F336W), appear weak in the optical band (F435W/F547M) and disappear in the IR band (F160W). The black strips in the F336W mosaic are the regions which are just covered by one dithered exposure and are simply removed to avoid the contamination from cosmic-rays. The black dots in the F160W mosaic are the due to ‘death star’ feature in the WFC3 /IR camera. The green lines in the top left panel represent parts of an intensity isophote with the major-axis radius of  $180''$ , while the cyan ellipse represents the isophote with the major-axis radius of  $90''$ .

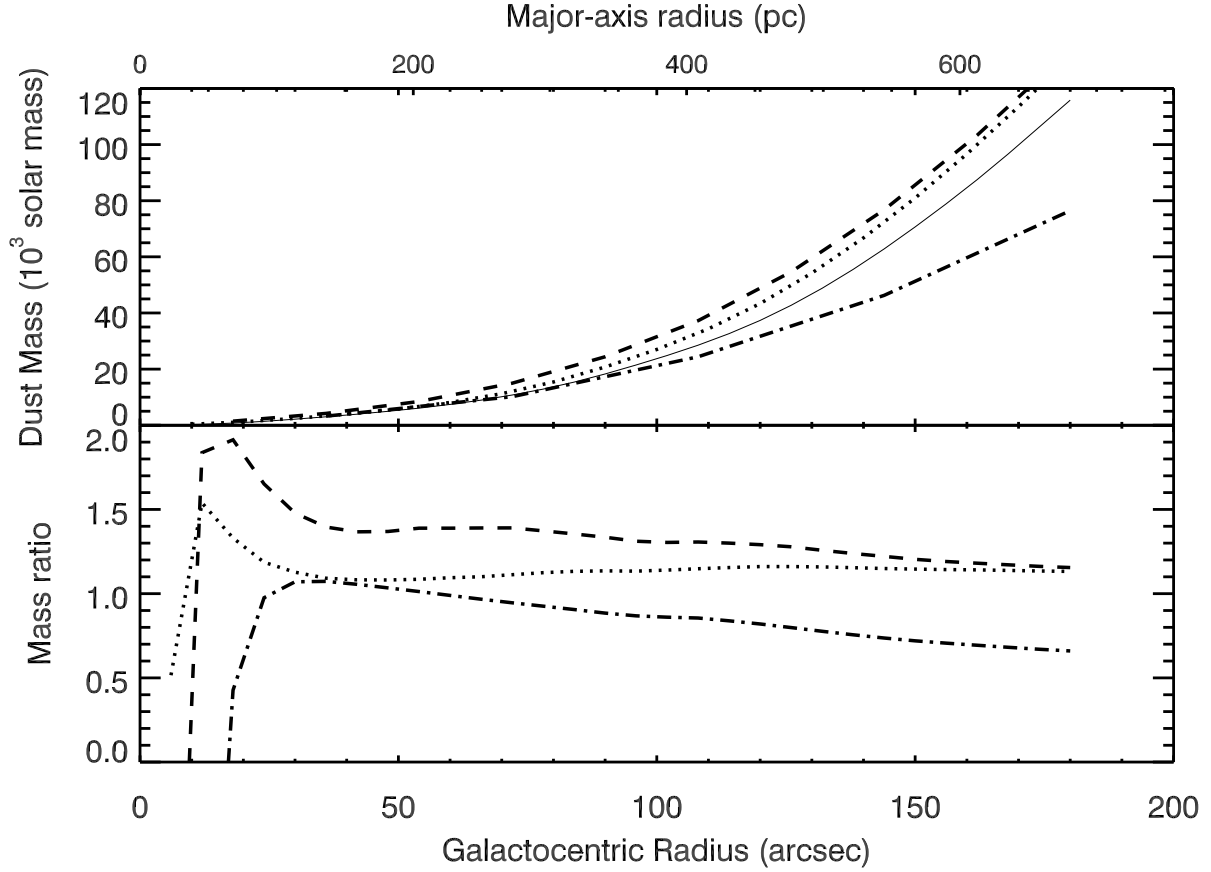


Fig. 2.— Top Panel: the enclosed dust mass as a function of the galactocentric radius estimated from the four dust mass surface density map: Groves et al. (2012) (solid), low/high resolution versions in Draine et al. (2014) (dashed/dotted) and Viaene et al. (2014) (dash dot). Bottom Panel: the estimated enclosed dust mass ratios of Draine et al. (2014) and Viaene et al. (2014) to Groves et al. (2012). The rest is the same as those in the top panel.



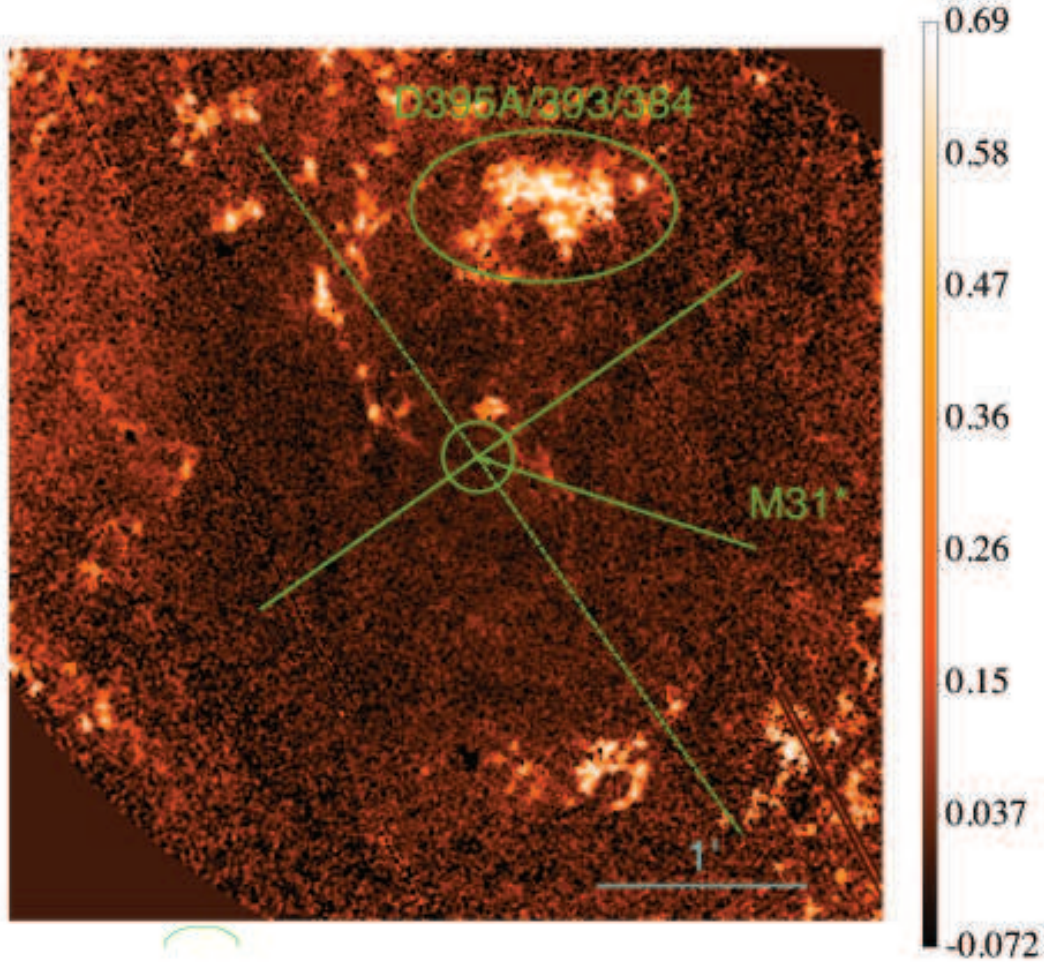


Fig. 3.— The spatial distribution of the extinction ( $A_{547M}$ ) in the central  $250'' \times 250''$  region of M31. The green circle shows the central  $10''$  around M31\* and the arrow points to M31\*; the dashed and solid green lines represent the major and minor axes of the M31 bulge; the green ellipse outlines D395A/393/384 studied by Melchior et al. (2000).

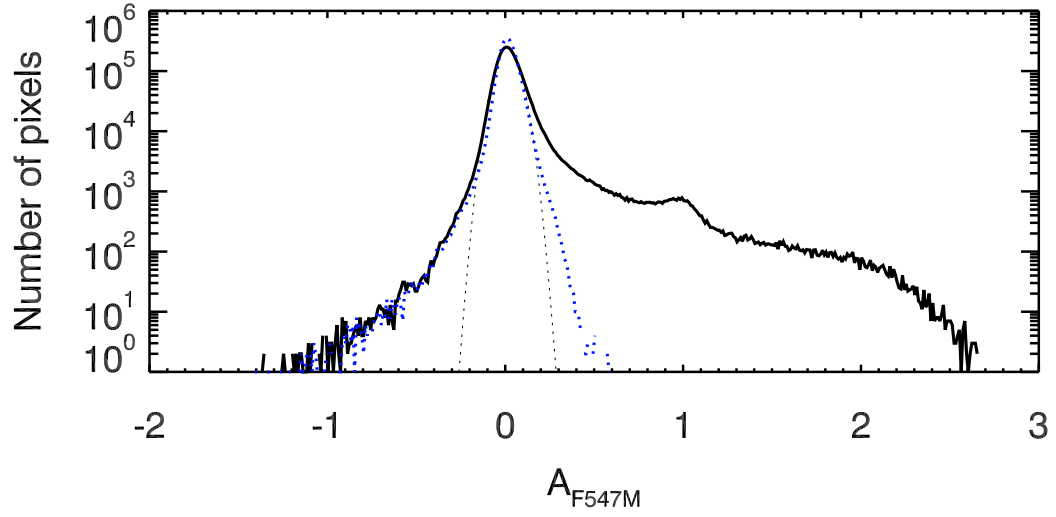


Fig. 4.—  $A_{F547M}$  distribution with a binsize of 0.01 mag. The black solid and blue dotted curves are for the extinction maps with spatially-varying  $f$  and fixed  $f=1$ , respectively. The latter assumes that all the dusty clumps are in front of the M31 bulge. The black curve near zero can be well characterized with a Gaussian function which centers at 0.014 and has a dispersion of  $\delta A_{F547M}=0.055$  (black dotted line).

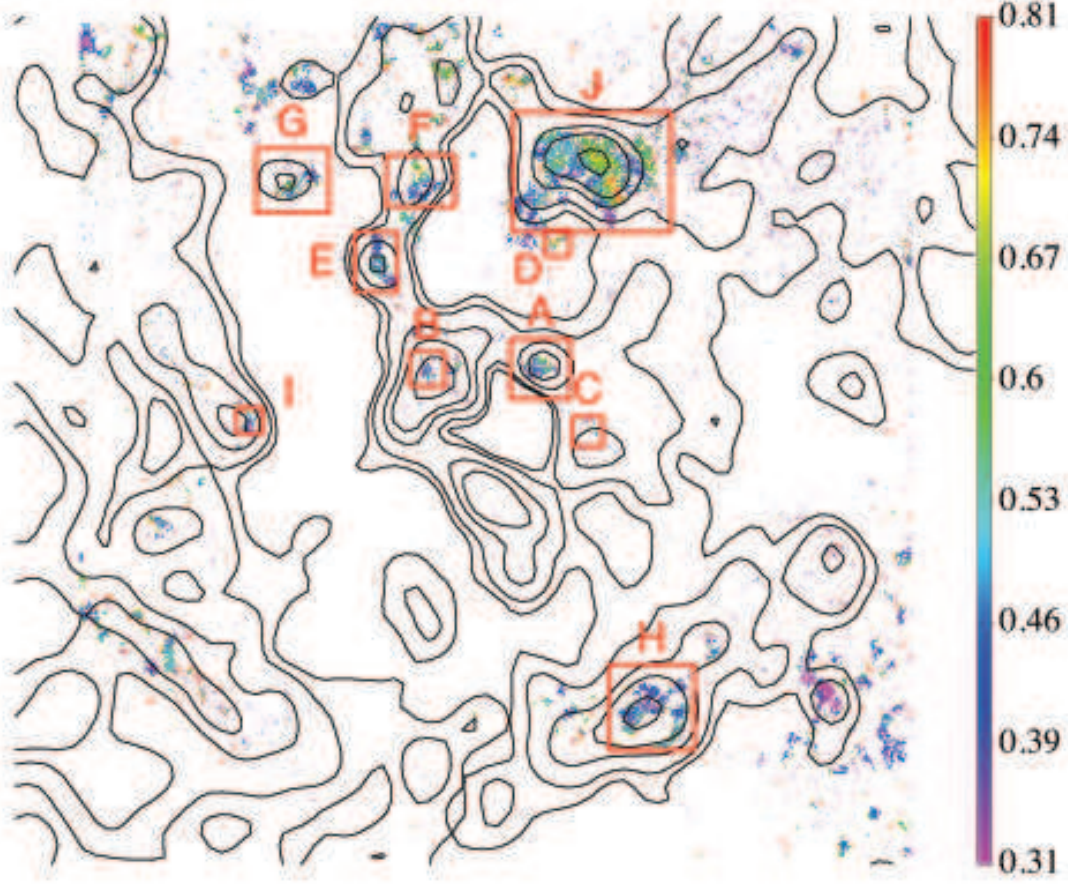


Fig. 5.— The spatial distribution of the fraction of obscured starlight,  $f$ , for the pixels with  $A_{F547M} > 3\delta A_{F547M}$ , overlaid with the contours from *Spitzer*/IRAC  $8\ \mu\text{m}$  ‘dust-only’ image. Regions, ‘A’ to ‘J’, are selected to calculate the mean and standard deviation of  $f$ , which are listed in Table 2.

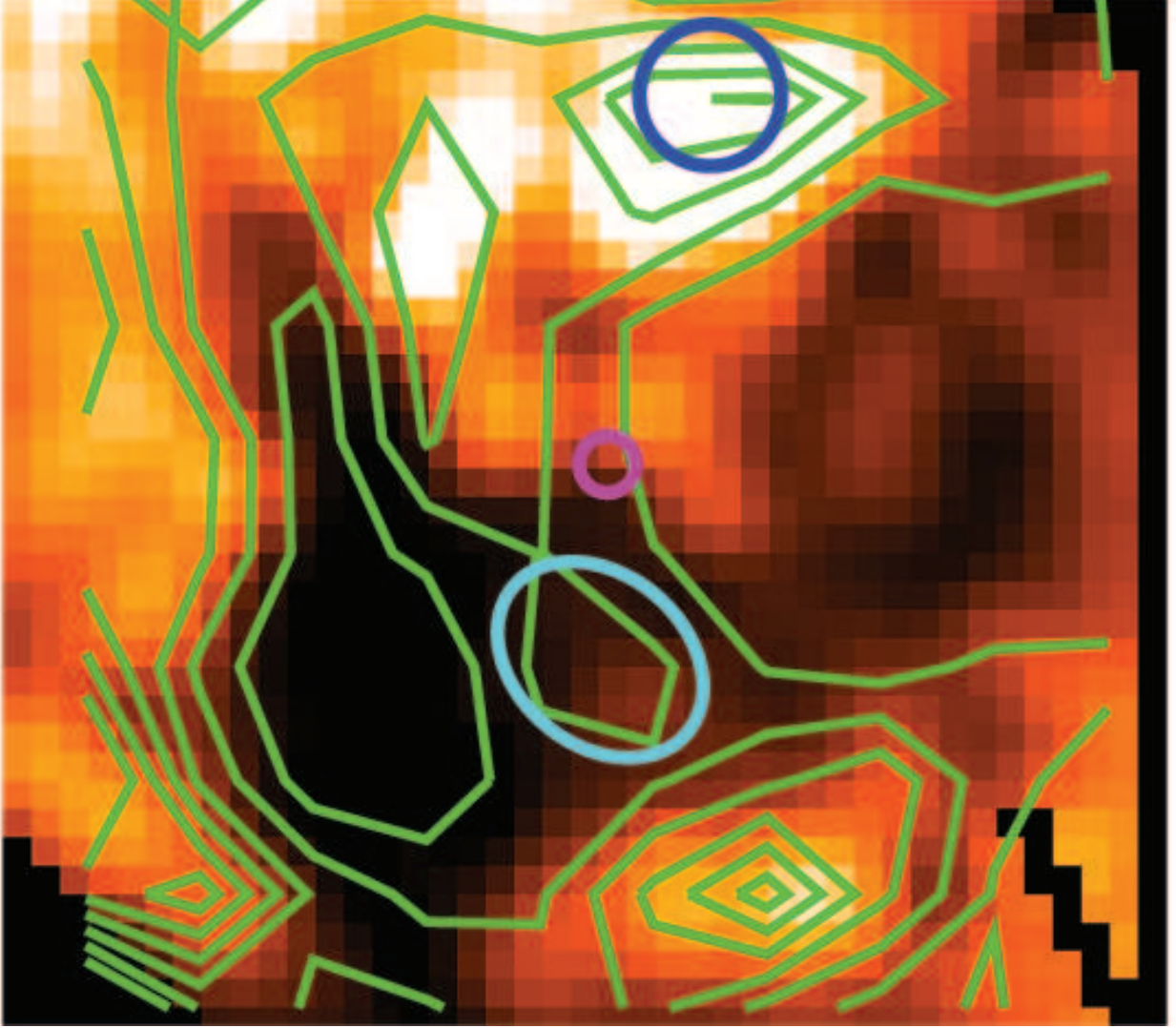


Fig. 6.— The dust mass surface density map from our extinction map, with a pixel size of  $6''$  (color image), compared with the (green) contours from the dust mass map of Groves et al. (2012). The magenta circle marks the center of M31 and the blue circle indicates D395A/D393/D384. The two dust maps appear similar in morphology, showing dust filaments and low-extinction patches to both east and west of M31\*. The cyan ellipse indicates one dusty clump,  $30''$  (i.e.,  $\sim 120$  pc) southeast of M31\*, which has been detected in the CO observations, but should be on the far side of the M31 bulge (Melchior & Combes 2013).



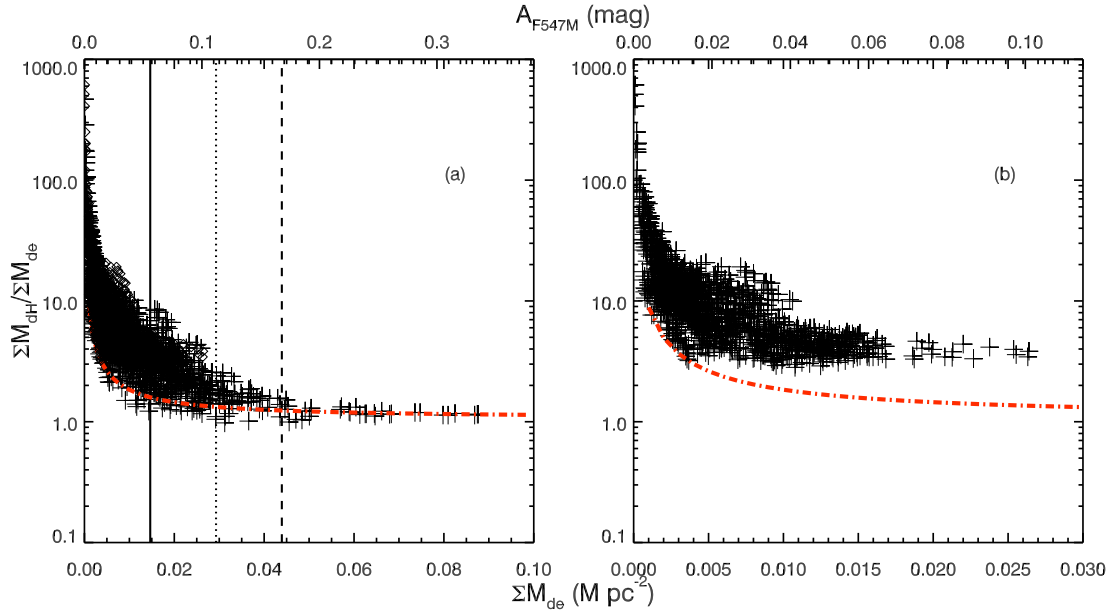


Fig. 7.— The pixel-by-pixel dust mass surface density ratio of the *Herschel* data ( $\Sigma M_{dH}$ ) to our extinction-inferred map ( $\Sigma M_{de}$ ) with (a) spatially-varying  $f$  and (b) fixed  $f=1$  as a function of  $\Sigma M_{de}$ . The abscissa axis ranges of these two plots are different. In panel (a), the solid, dotted and dashed lines represent one, two and three times the uncertainty of our map. The red dot dashed lines in both panels represent the same linear fit between  $\Sigma M_{dH}$  and  $\Sigma M_{de}$  for pixels with  $M_{de} > 3\delta M_{de}$  in the map with spatially-varying  $f$  (see § 4.2).

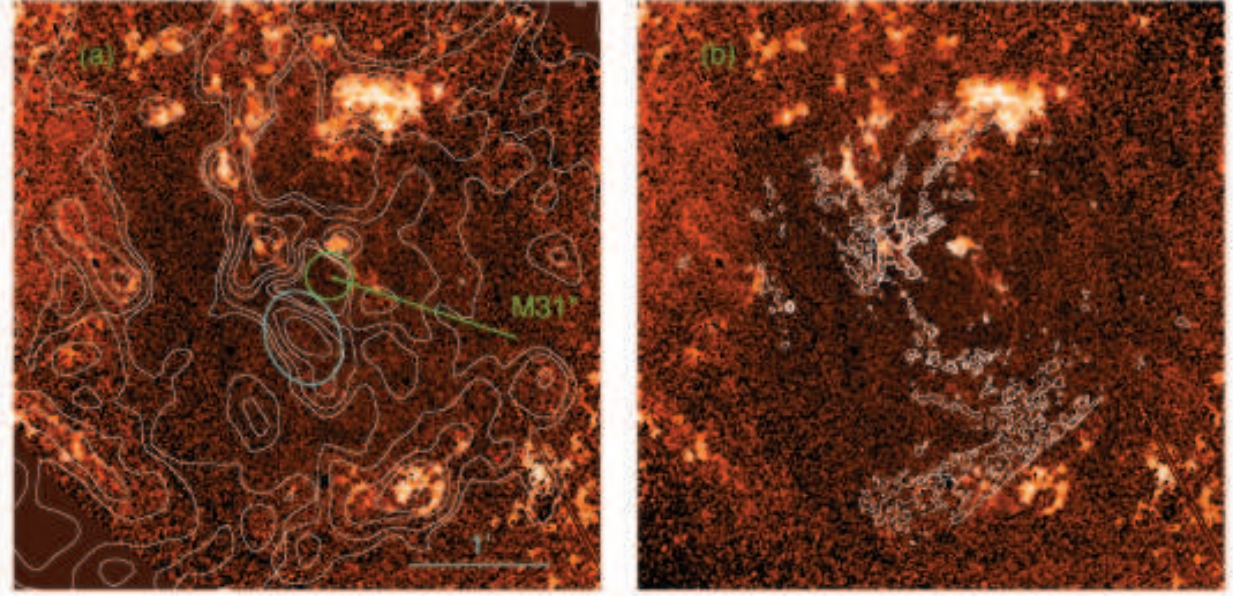


Fig. 8.— The spatial distribution of the extinction ( $A_{547M}$ ) in the central  $250'' \times 250''$  region of M31, overlaid with the contours from (a) *Spitzer*/IRAC  $8.0 \mu\text{m}$  ‘dust-only’ image and (b)  $\text{H}\alpha + [\text{N II}]$  emission from HST imaging (Li et al. 2016, in preparation). In (a), the green circle shows the central  $10''$  around M31\*; the cyan ellipse to the southeast of M31\* marks a dusty clump detected in the *Spitzer*/IRAC  $8 \mu\text{m}$  observations, but without any apparent extinction of the starlight from the M31 bulge.



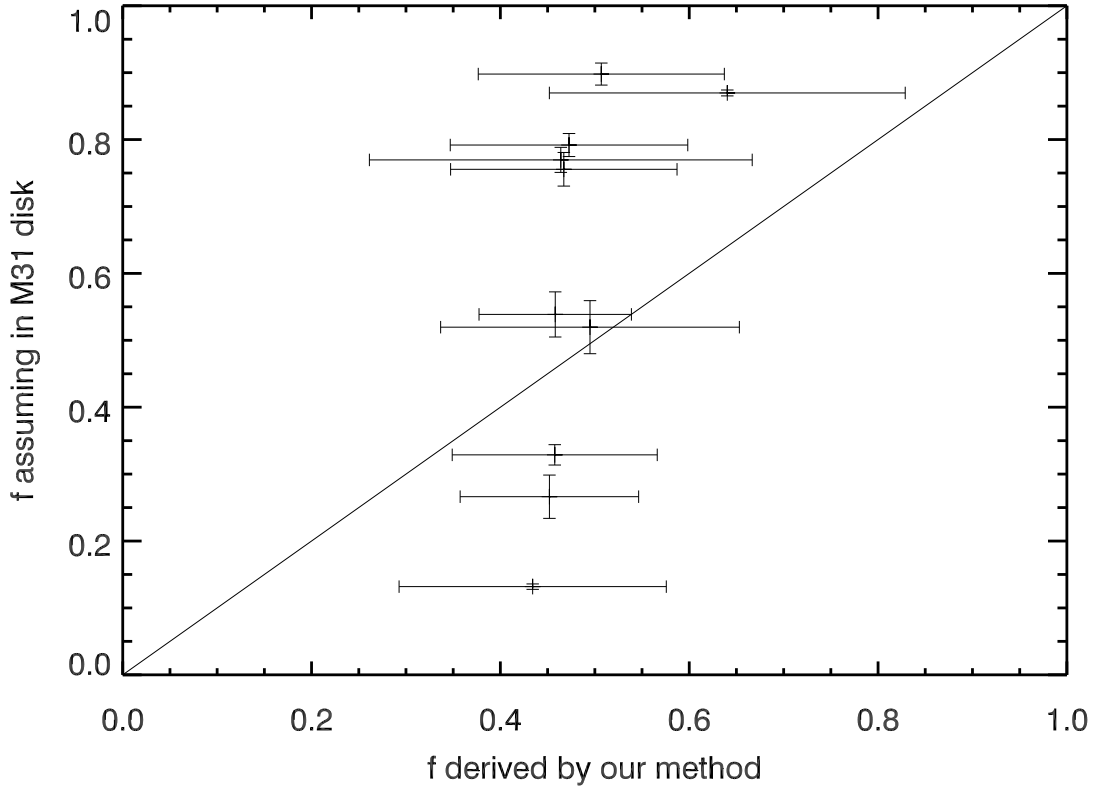


Fig. 9.— Comparison of the obscured fraction  $f$  for the dusty clumps in Fig. 5 between the cases of using our method and the case of assuming that they are located in the same plane as the M31 disk.

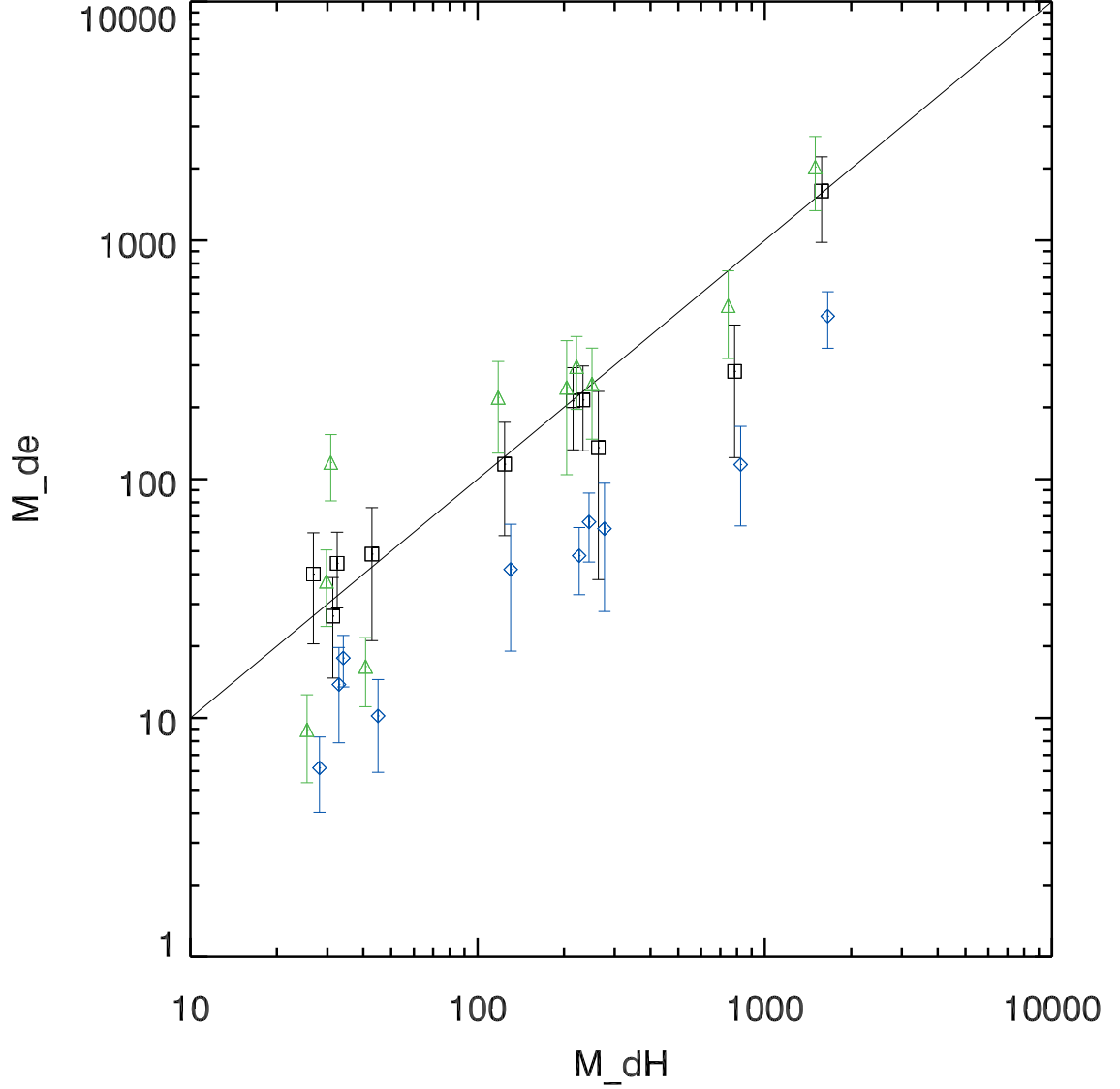


Fig. 10.— Comparison of the masses of the dusty clumps (in units of  $M_{\odot}$ ) in Fig. 5 from the extinction map ( $M_{de}$ ) with spatially-varying  $f$  (black squares) or fixed  $f=1$  (blue diamonds) with those from the *Herschel* data ( $M_{dH}$ ). The green triangles represent the masses of clumps, assuming that they were in the Virgo cluster, derived by our method with spatially-varying  $f$ . The blue diamonds and green triangles have been slightly shifted along the abscissa axis for better demonstration.

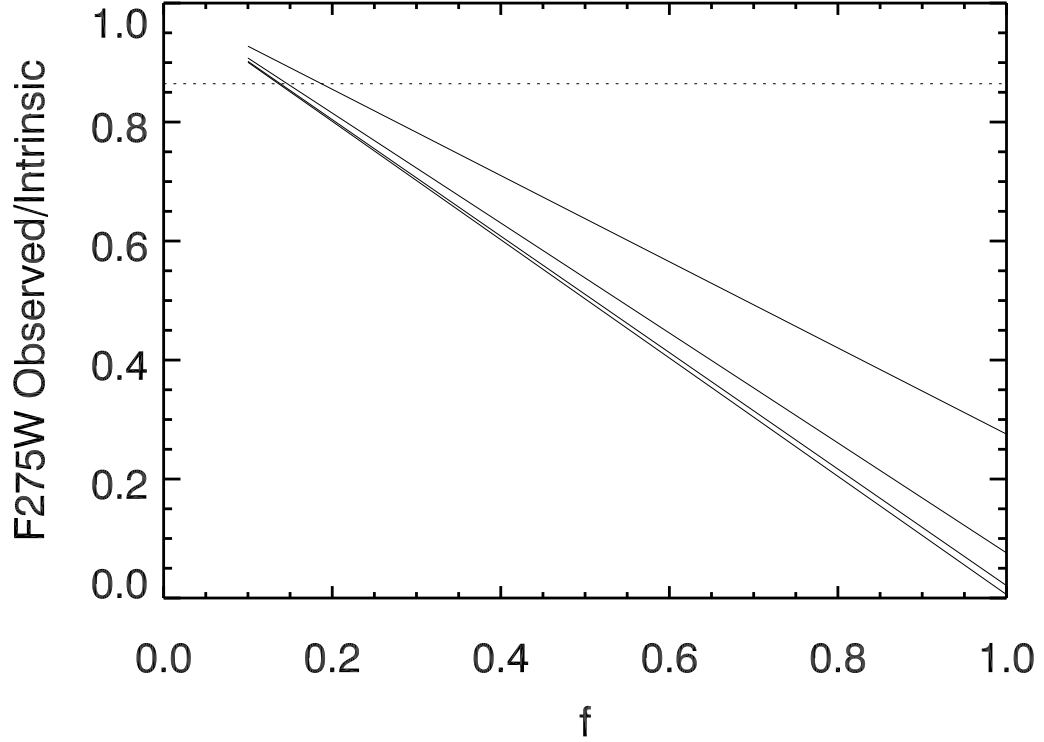


Fig. 11.— Demonstration of the ratio of the observed to intrinsic F275W intensities as a function of  $f$  for a molecular cloud with  $A_{F547M}=0.5, 1, 1.5$  and  $2$  mag (from top to bottom). The horizontal dashed line marks the photometric uncertainty at F275W band for one pixel of our mosaic (13.5%, which consists of 13.1% statistical uncertainty and 3.5% systematic uncertainty, see Table 1 of Dong et al. 2015) from 1.

Table 2.  $f$  values and off-M31\* Distances of the Dusty Clumps

ID	$f$	Projected Distance	Radial Distance (pc) <sup>a</sup>
A	$0.47 \pm 0.13$	$13''$ (52 pc)	$7.4 \pm 26.3$
B	$0.46 \pm 0.11$	$32''$ (123 pc)	$16.3 \pm 37.9$
C	$0.46 \pm 0.20$	$19''$ (71 pc)	$10.7 \pm 55.3$
D	$0.64 \pm 0.19$	$51''$ (196 pc)	$-62.4 \pm 101.6$
E	$0.46 \pm 0.08$	$64''$ (242 pc)	$23.0 \pm 41.1$
F	$0.47 \pm 0.12$	$76''$ (289 pc)	$20.1 \pm 67.7$
G	$0.49 \pm 0.16$	$99''$ (374 pc)	$5.2 \pm 102.1$
H	$0.45 \pm 0.09$	$95''$ (362 pc)	$31.7 \pm 59.4$
I	$0.43 \pm 0.14$	$83''$ (314 pc)	$40.0 \pm 85.2$
J	$0.51 \pm 0.13$	$74''$ (283 pc)	$-1.7 \pm 72.7$

Note. — a) the positive (negative) values mean that the clumps are behind (in front of) the plane of M31\*.

Table 3. The Mass of Dusty Clumps

ID	$M^a$	$M_{f=1}^b$	$M_{Herschel}^c$	$M_{Virgo}^d$
A	116±58	42±23	124	220±91
B	40±20	6±2	27	9±3
C	27±12	14±6	31	37±13
D	44±16	18±4	32	117±36
E	213±80	48±15	215	242±138
F	215±83	66±21	233	296±100
G	136±98	62±34	263	251±103
H	283±159	115±51	785	533±213
I	49±27	10±4	43	16±5
J	1609±629	482±128	1578	2028±695

Note. — the dust mass in units of solar mass a) derived from the attenuation map with spatially varied  $f$ ; b) derived from the attenuation map with fixed  $f=1$ ; c) measured from the *Herschel* data; d) measured from the attenuation map with spatially varied  $f$ , but assuming that the clumps were in the Virgo Cluster.